Composites Part B 272 (2024) 111208

Contents lists available at ScienceDirect

Composites Part B

journal homepage: www.elsevier.com/locate/compositesb

Full-field characterizations of additively manufactured composite cellular structures

Anil Singh [a], Behrad Koohbor [b], George Youssef [a,*]

[a] Experimental Mechanics Laboratory, Mechanical Engineering Department, San Diego State University, San Diego, CA, USA
[b] Department of Mechanical Engineering, Rowan University, Glassboro, NJ, USA

ARTICLE INFO

Handling Editor: Dr Uday Vaidya

Keywords:
3D printed composites
Quasi-static compression
Impact loading
Digital image correlation
Strain localization

ABSTRACT

Honeycomb structures possess unique mechanical and structural behaviors, including high specific strength, superior energy absorption, and potential for multifunctionality. The advantages of such structures are bolstered by their realization through additive manufacturing, enabling cellular geometries beyond traditionally fabricated hexagons and facilitating a pathway for hybridization using composite materials to tune the response. This research synthesized photocurable, particulate-reinforced resins using mechanically compliant matrix and glass microballoons reinforcement. The modified resins were used to additively manufacture lattice structures with circular and hexagonal unit cell geometries at different glass microballoons reinforcement weight ratios, ranging from neat to 20 *wt.*%. The 3D printed structures were tested under quasi-static and impact loading scenarios to elucidate the interrelationships between the cell geometry, induced deformations, and strain rates. The mechanical testing was coupled with digital image correlation (DIC) to reveal the deformation-geometry interrelationship on the global (macroscale) and local (mesoscale) levels. The multiscale analyses allowed for extensive characterization of the effect of cell geometry and increased weight reinforcement on the mechanical response at a global, sub-cellular, and cellular level, *i.e.*, elucidating the hierarchical dependency. The novelty leading to the current study stems from probing and revealing the deformation state of cellular structures subjected to two loading scenarios using DIC. This study intended to provide mechanistic insights for engineering lattice structures for impact mitigation applications by offering a viable approach to additive manufacturing composite materials.

1. Introduction

The structural response of honeycomb cores for composite sandwich structures is a symbiotic interplay between the geometry of the unit cell and the properties of the materials entrapped in the cell walls. On the one hand, the hexagonal unit cell geometry is ubiquitous in aerospace composites due to the desirable in-plane and out-of-plane properties, including ample free space and lightweight [1–5]. Nonetheless, hexagon-based cores are plagued by sharp transitions between the vertices, resulting in stress concentrations or strain localizations that lead to failure [6]. On the other hand, circular cell geometry remedies the geometrical shortcomings of hexagonal counterparts since the curvature is continuous along the cell perimeter. This comes, however, at a manufacturing disadvantage stemming from the existing streamlined approach of fabricating hexagonal honeycombs. The paradox of the divergent requirements is manifested at an opportune time in the engineering space, given the influx of research focusing on additive manufacturing of composite materials, irrespective of the geometry.

Honeycomb cores, initially inspired by natural structures, are frequently used to manufacture composite sandwich structures consisting of stiff and strong skins and lightweight and flexible cores. While traditional honeycomb cores have been vigorously investigated, showing favorable mechanical and structural behavior, the typical hexagonal geometry has been challenged in recent years by exploring variations of the hexagonal unit cell and extending to other geometries, *e.g.*, cylindrical and reentrant hexagons, as well as the effect of reinforcing the cell walls [7–11]. For example, Pagliocca et al. studied the in-plane mechanical and failure responses of syntactic honeycombs [12] that were mold cast with different volume fractions of reinforcing hollow glass beads, cell wall thickness, and density gradients. Pagliocca and collaborators showed heterogeneous strain localization at the cell hinges, leading to brittle fracture; nonetheless, the density gradation

* Corresponding author.
E-mail address: gyoussef@sdsu.edu (G. Youssef).

https://doi.org/10.1016/j.compositesb.2024.111208
Received 23 June 2023; Received in revised form 3 January 2024; Accepted 7 January 2024
Available online 9 January 2024

positively influenced the mechanical behavior [12]. Xu et al. demonstrated that the peak and plateau stresses increased, *i.e.*, there was improvement in the mechanical behavior in functionally graded, foam-filled reentrant aluminum honeycomb structures [13]. They also reported an enhanced energy absorption performance compared to the unfilled counterparts [13]. Liu et al. also investigated the impact efficacy and failure mechanism of reentrant honeycomb structures using experimental and computational approaches [11]. Liu et al. prepared the reentrant honeycombs using hot-pressed carbon fiber/epoxy prepreg, where the negative reentrant configuration exhibited improved impact resistance [11]. Reentrant honeycombs are characterized by a negative Poisson's ratio, resulting in enhanced indentation resistance, stiffness, and energy absorption [14–16]. Song et al. fabricated and mechanically characterized composites-based interlocked triangular honeycomb sandwich structures [17], reporting a >20 % increase in specific strength and nearly threefold improvement in specific stiffness over traditional counterparts. In all, prior research recently affirmed the importance of honeycomb structures in various loading scenarios, highlighting the positive influence of tailored geometry and composite materials on the overall performance.

Particulate composite materials (particle-reinforced composites), especially those comprising ceramics reinforcement and polymer matrix, constitute an important class of engineering materials since the properties can be readily tuned to match demanding application requirements [18,19]. The reinforcement phase (*i.e.*, particles, short fibers, or flakes), irrespective of the geometry, size, ratio, and source, contributes to changes in stiffness (*e.g.*, storage and loss moduli), strength, and ductility using ceramic particles such as glass beads, carbon ash, or clay particles, to name a few examples of common reinforcements [18,20,21]. The polymer matrix is the primary phase, providing the overall form of composites by enclosing or concealing the embedded phase within [22–24]; hence, the matrix transfers and shares the load with the secondary reinforcement phase. It is then imperative to note that the selection of the polymer for the matrix phase is crucial since it maps directly to the geometrical, environmental (*e.g.*, recyclability), thermal, and hygrothermal stability of the composite in real-life deployments [25]. In the recent past, thermoplastic and thermoset polymers have been used as composite matrices to manage mechanical behavior. Thermosetting polymer matrices encompass many resins and epoxies, creating composite materials and structures for aerospace and construction applications [26–28]. Common thermoplastic polymers, such as polyamides and polystyrene, have also been reported [29–34]. The choice of the polymer matrix is further restricted when considering advanced manufacturing techniques, such as automated fiber placement or 3D additive manufacturing [33]. In the latter case, the curing approach additionally limits the choice of polymers based on the source of curing energy, *e.g.*, thermal or photonic [33,35–37]. Thermally cured resins and epoxies are generally more resilient than their ultraviolet-cured counterparts based on the molecular structure [28]. Nonetheless, ultraviolet-cured resins are becoming essential for accelerated development in 3D printing since they are readily available, easily formulated, and quickly modifiable [36,38]. The importance and tailor-ability of particle-reinforced composite material systems motivate this current study.

A keen interest in additive manufacturing is manifested in recent literature based on printable materials and the availability of advanced equipment to achieve multiscale tuning of material and structural responses [3–5,36–38]. Such interest is also fueled by the transition of lab-scale prototypes to application-scale deployable structures, requiring rigorous quality and performance control to avoid premature failures. However, a focus on extending the applicability of existing and mature 3D printing approaches, *e.g.*, vat photopolymerization, is needed to sustain such growth in interest and utility. Vat photopolymerization is an agile 3D printing process based on photocurable resins that are easily amendable to composites, especially particle-reinforced polymers [2,4,5]. Commercially available resins exhibit a broad range of mechanical properties, including glass-like and elastomer-like materials, suitable for various applications such as consumer goods or medical devices. In addition to improving the printing parameters (*e.g.*, print speed, layer height, resin viscosity, *etc.*), recent research also focused on enhancing the mechanical properties (*e.g.*, adding glass microballoons, chopped fibers, carbon nanotubes, or graphene flakes) or multifunctionality (including printing of multiphasic materials consisting of electroactive polymer, magnetic particles, and mechanical scaffolding) by creating composite material systems. Notably, several manufacturing challenges arise when 3D printing particulate composite materials, including controlling the geometrical accuracy of parts and structures, as well as reducing postprocessing steps before deployment [5,39]. The problem is further exaggerated if flexible resins with elastomeric properties are used in 3D printing due to their high viscosity, temperature and moisture sensitivity, and excessive elasticity. Some additional common challenges, translated from conventional manufacturing techniques, include the settlement of reinforcement particles before curing, resulting in nonuniform distribution, agglomeration due to size and stiction, and premature gelation or infusion of the matrix during the mixture or transfer processes. Axiomatically, these debilitating challenges hinder the rapid infiltration of 3D printable composites into the application space. Hence, an emphasis is placed herein on the process-property-structure of printed honeycombs using ceramic-reinforced photocurable flexible resin.

The overarching objective of the research leading to this report is to reveal the structural and mechanical response of honeycombs with hexagonal and circular cell geometries under in-plane quasi-static and impact loading conditions. The honeycombs were manufactured using a 3D printing, vat photopolymerization process based on tuning the properties of a mechanically compliant stock resin with glass microballoons reinforcement. The additively manufactured honeycombs were mechanically characterized using a standard load frame and a modified drop weight impact machine concurrently and separately retrofitted with corresponding image recording capabilities at different acquisition rates. The photographic footage was analyzed using digital image correlation (DIC) to elucidate the local mechanical response of the unit cells as a function of unit cell geometry, reinforcement ratio, and deformation rate.

2. Materials and methods

Two honeycomb structures with cylindrical and hexagonal cell geometries were 3D printed and characterized to investigate material-structure-deformation interrelationships at the structural (macro) and cell (meso) scales. Vat photopolymerization (VPP) additive manufacturing was used in this research based on a trifold rationale. First, the geometric stability of VPP-manufactured components facilitates the fabrication of complex shapes, such as the combs printed herein with different geometries. Second, VPP enables the use of photocurable materials with a wide range of mechanical properties, from compliant to rigid polymers. A flexible resin (Resione F69) was used herein to explore the hyperelastic behavior of ordered cellular structures under compressive loading at different strain rates. Third, VPP is amendable to further tuning the mechanical properties of printable materials by hybridizing stock resins with reinforcements, *i.e.*, the realization of printed particulate-composite materials. Thus, the study fabricated composite honeycomb structures using stock resin loaded with different weight ratios (5 *wt.*%, 10 *wt.*%, and 20 *wt.*%) of hollow glass microspheres (Supelco 440345-500g SiO_2 Glass Spheres, Ø = 9–13 μm).

The sample preparation process through VPP consisted of five stages (Fig. 1). The first was configuration design and modeling for the unit cell layout of each structure. Irrespective of the unit cell geometry, the comb structures were modeled with stagnantly arranged cells into nine rows and eight columns, which were enclosed by an exterior wall to ensure uniform load distribution (*i.e.*, avoid premature buckling of the cell edges in contact with the compression platens). In the second stage, the

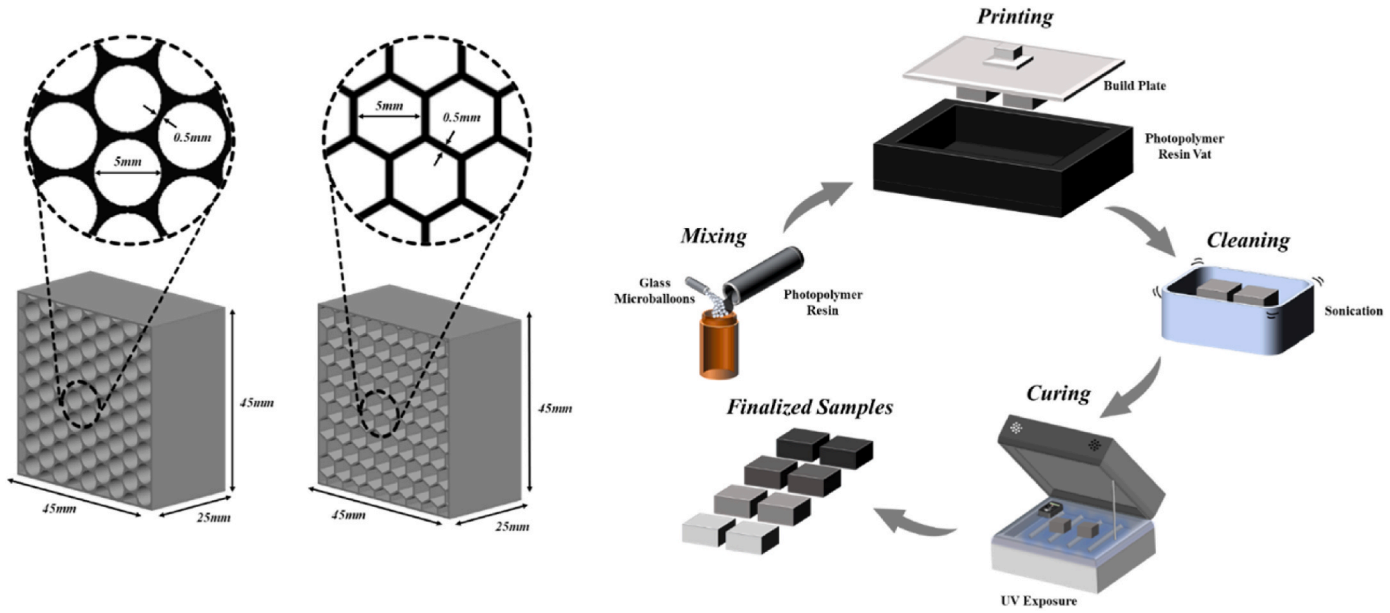

Fig. 1. Sample design and fabrication process for additively manufacturing glass-reinforced cylindrical and hexagonal honeycombs using mechanically compliant photocurable resins and vat photopolymerization 3D printing process.

stock resin was mixed with the glass microballoons, followed by 10 min of manual stirring in an amber jar and 20 min of sonication. The microballoons remained undamaged during the mixing process, which was subsequently confirmed by scanning electron microscopy (SEM) that revealed intact microballoons present in printed structures [12,40]. SEM micrographs of the printed and tested structures are included in the *Supplementary Document.* Third was the fabrication of the lattice structures using a masked stereolithography 3D printer (Anycubic Photon S LCD Resin 3D Printer) based on the printing parameters reported previously in Ref. [40]. In the fourth stage, the excess resin was removed from the printed samples using compressed air (70 kPa), followed by 20 min of sonication in a cleaning solution (an equal mixture of water and isopropyl alcohol, and liquid detergent). Finally, the structures were exposed to ultraviolet radiation for 80 min before being conditioned in dark, ambient conditions for two weeks. Ten structures were 3D printed using the modified resin with different weight percent for quasi-static and impact testing.

Quasi-static testing (Fig. 2a) was performed using a 1 kN load frame (Instron 5843) at ambient conditions at a crosshead speed of 50 mm/min, equivalent to a global nominal strain rate of $\sim$0.02 s^{-1}. The compression loading course was imaged at a rate of 15 Hz using a Basler camera (Basler, acA1300-30gc) fitted with an objective lens (HAYEAR 10-300x), resulting in a 13.5 mm $\times$ 10 mm field of view of the front face of the sample. On the other hand, dynamic testing (Fig. 2b) was performed on a modified drop weight machine at an impact energy of 9.6 J by dropping a 950 g mass from a height of 103 cm. The flattop drop carriage was instrumented with a load cell to record the impact force at a sampling rate of 15 kHz while recording digital images using a high-speed camera (Photron FASTCAM SA1.1) fitted with a Nikkor 72 lens at a rate of 54000 fps.

The digital images from each loading scenario were analyzed using commercial digital image correlation software (Istra4D V4.9, Dantec Dynamics Inc.), and as such, a speckle pattern was applied via airbrush. DIC parameters were selected to accommodate the speckling pattern characteristic of the honeycomb. The *Supplementary Document* includes the first speckled image from each sample configuration, illustrating the quality of the speckle pattern. The optimized speckle pattern did not show signs of flaking and was observed to consistently deform with the sample under load. The quasi-static loading scenario was evaluated with a facet size of 21 pixels (172 μm) and grid spacing of 15 pixels (123 μm). A facet size of 31 pixels (167 μm) and a grid spacing of 9 pixels (48 μm) was used for the impact loading to account for high-speed imaging artifacts. In addition to calculating the strain distribution within the field of view, a representative unit cell was virtually instrumented using linear strain gauge objects (Fig. 3) to extract the kinematic parameters listed in Table 1, revealing insight into the deformations unique to each unit cell geometry and reinforcement weight ratio.

3. Results and discussion

This section is divided into two subsections, focusing on the mechanical testing at two different strain rates, namely quasi-static (Loading Scenario I) and drop-weight impact (Loading Scenario II). The rationale for such separation is the large volume of data and the various sample configurations considered herein. Honeycombs with circular and hexagonal unit cell geometries were printed using modified photocurable resin with glass microballoons reinforcement (0 *wt.%*, 5 *wt.%*, 10 *wt.%*, and 20 *wt.%*), which were also characterized as mentioned above.

3.1. Loading scenario I: quasi-static compression

Fig. 4 comprises composite contour plots of the in-plane strain components, including axial, lateral, and shear (ε_{YY}, ε_{XX}, and ε_{XY}, respectively), for honeycombs with cylindrical and hexagonal unit cell geometries printed with the neat and 20 *wt.*% of the glass microballoons. Similar figures are included in the *Supplementary Document* for the remaining weight reinforcement configurations (*i.e.*, 5 *wt.*% and 10 *wt.* %) to avoid repetition of observations and discussion. The contour plots in Fig. 4 correspond to initial undeformed (column 1) and deformed structures at 5 % and 10 % global strains in columns 2 and 3, respectively. The axial strain contour plots reveal four characteristics of the state of deformation that are collectively persistent within the observable unit cells in the field of view. First, axial strains localized in tension at the connecting points (*i.e.,* nodes) and in compression in the ligands defining the unit cells (*i.e.,* hinges), irrespective of cell geometry or reinforcing weight ratio. For example, at 10 % global strain, the localized tensile strain at the nodes for the circular unit cells ranged between 0.13 % and 1.90 %, considering the trackable nodes within the field of view based on the imaged unit cells. The hexagonal unit cells reported

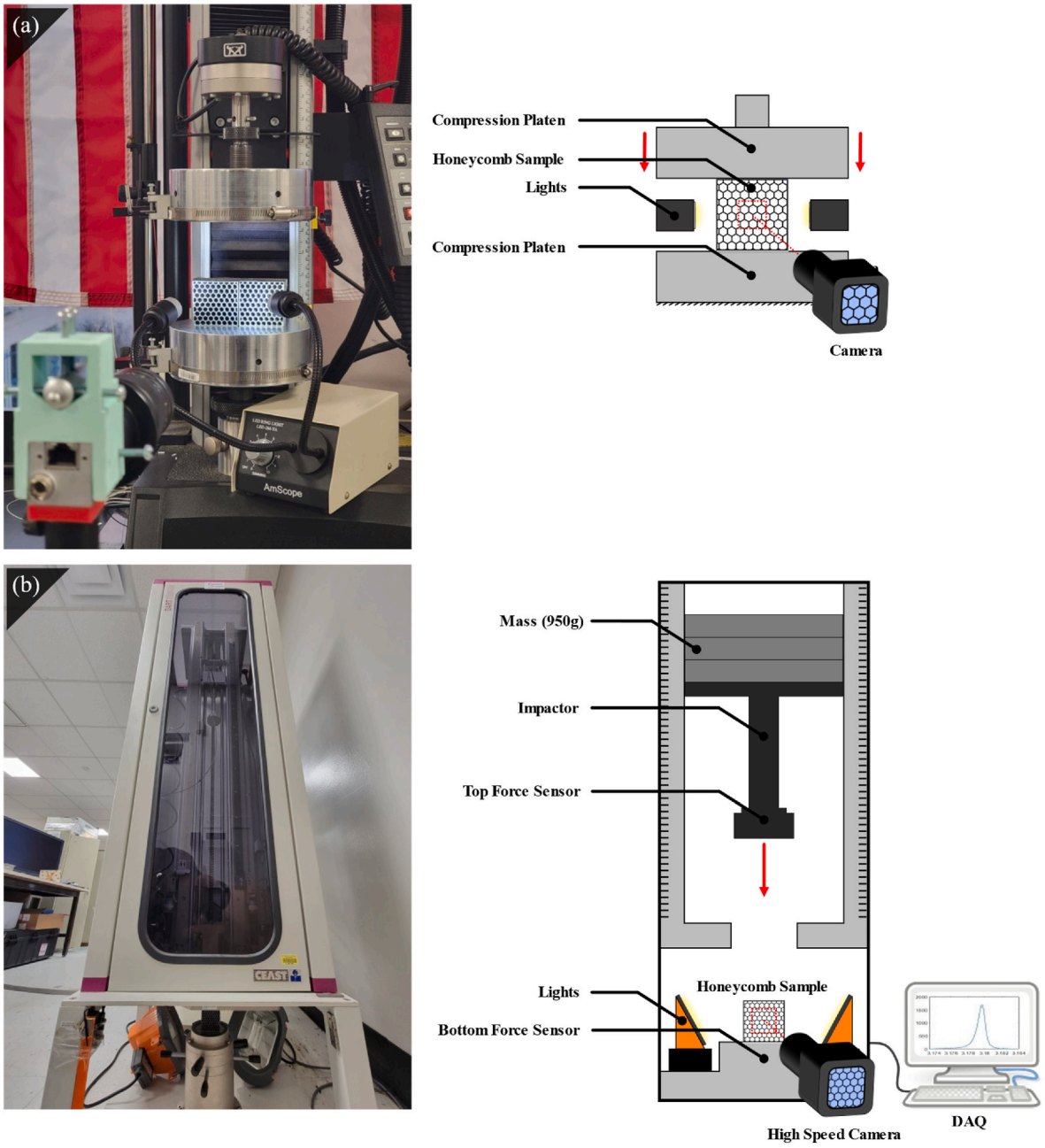

Fig. 2. Experimental setups used in characterizing the mechanical responses of additively manufactured composite honeycomb structures under (a) quasi-static using 1 kN standard load frame and (b) impact using modified drop-weight tower while acquiring images for ex-situ full field analyses.

localized tensile strains at similar locations, ranging between 0.81 % and 2.64 %. Similarly, the localized compressive strain within the ligands varied from −0.39 % to −3.37 % and −0.09 % to −3.29 % for the cylindrical and hexagonal honeycombs, respectively. Second, the unit cell geometry contributed to the level of generated axial strains, where the cylindrical honeycombs generally reported a broader range of ligand compressive strains than their hexagonal counterparts, regardless of the reinforcement weight ratio. Conversely, the hexagonal structures reported significant variations in the nodal tensile strains compared to the cylindrical structures. The reinforcing phase had a major effect on the reported axial strains, where a 20 % increase in the reinforcement ratio resulted in an 82 %, on average, increase in the generated strains. The increase in the induced strains is associated with matrix-reinforcement bonding issues, resulting in pseudo-foaming that caused increased deformation with an increase in reinforcement ratio. The final observation from the strain contour plots in Fig. 4 is the strain distribution within a unit cell, where the laterally oriented ligands sustained notable deformations while their axially positioned counterparts are nearly strain-free. This strain distribution is attributed to the global structural deformation, where the relative motions of the connected unit cells must yield physically permissible conditions that accommodate cell rotation, bending, stretching, and collapse as the applied load increases.

The mechanistic insights derived from the axial strain distribution are also manifested in the lateral and shear strains contour plots reported in Fig. 4. Regardless of the unit cell geometry and the reinforcement weight ratio, the lateral strain inherits the attributes of the axial companion strains except for a sense reversal. Ligands are strained in tension while the nodes are under compression. The relationship between the applied axial deformation and the accompanying lateral strains is attributed to the in-plane loading of honeycomb structures,

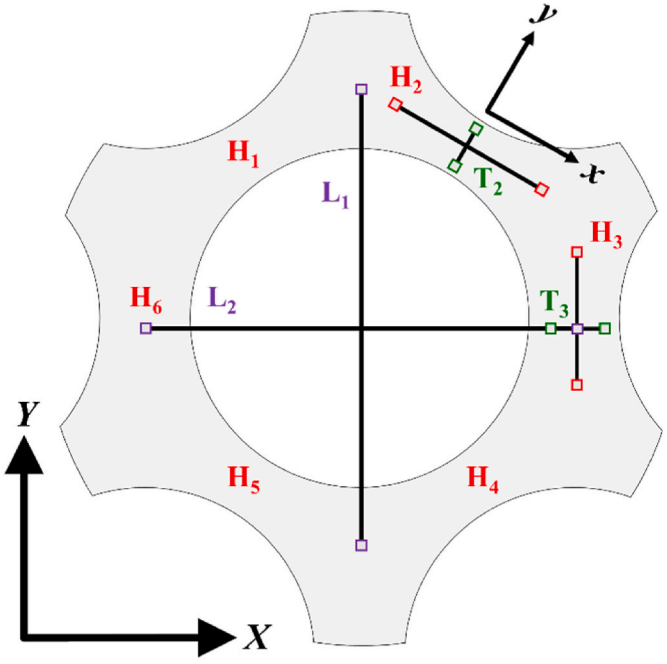

Fig. 3. Diagram of virtual instrumentation strategy for extracting resolved deformation characteristics (Table 1) from representative cylindrical unit cell.

Table 1
Strain metrics extracted from DIC analysis (also see Fig. 3).

Strain Metrics	Symbol	Virtual Gauge
Lateral engineering strain	ε_{XX}	
Axial engineering strain	ε_{YY}	Overall Correlation Mask
Shear engineering strain	ε_{XY}	
Axial cell strain	ε_a	L_1
Lateral cell strain	ε_l	L_2
Axial hinge strain	ε_{yy}	H_2, H_3
Lateral hinge strain	ε_{xx}	T_2, T_3

where longitudinally stacked cells contract while extending laterally. Notably, the cell geometry is also correlated with the strain distribution within an individual ligand. Lateral strain localized in the pseudo-ligand of the cylindrical honeycombs, whereas it dilated throughout the struts of the hexagonal unit cells. Congruently, the development of shear strains in the cylindrical and hexagonal honeycomb structures is a byproduct of the axial and lateral state of strains discussed above, such that the shear strain accommodates the bending, rotation, and stretching of the ligands defining the unit cells. The combined effect of the localized deformation within the ligands is manifested as the complementary distribution of shear strains around a unit cell. For example, a positive shear strain on one diagonal of a cell in the cylindrical combs is coupled with the complementary shear on the opposing diagonal. The effect of cell geometry and reinforcing weight ratio on the magnitude of the shear strains is consistent with their axial and lateral counterparts.

With an emphasis on the cellular level, the axial and lateral deformations (ε_a and ε_l, respectively) of a unit cell were extracted by defining virtual line gauges that extend in the corresponding directions (Fig. 3). Fig. 5 is a plot of the dependence of the lateral deformations of the unit cell on the axial counterparts, signifying a quasi-linear relationship. The rationale for ascribing a quasi-linear behavior to the relationship between the lateral and axial deformations stems from the intrinsic nonlinear behavior of the photocurable flexible resin used in fabricating the 3D printed structures. Another reason for this quasi-linear behavior is the deformation mechanisms associated with the physical movement of the unit cells within the structure. The slope of such a relationship is representative of the average apparent strain ratio of the structure at global scales, which exhibits a strong reliance on the cell geometry but a mild correlation with the reinforcing weight ratio of the glass microballoons. The strain ratios for the cylindrical honeycombs are determined as 0.295 and 0.265 based on the slope of the line defining the relationship between lateral and axial strains for 0 *wt.*% and 20 *wt.*%, and 0.452 for both reinforcement weight ratios of the hexagonal structures. The resolved average values of the cell-level strain ratio illustrate a geometry-induced correspondence. Axial movement of the oblique ligands in the hexagonal unit cell directly translates into lateral movement of the vertical struts. That is not the case in the cylindrical unit cell, where the continuous curvature of the circle plays a role in the apparent slowing down of lateral movement in relation to the applied axial deformation such that pseudo-ligands must first develop due to the strategic strain localization within the unit cell structure, as discussed next and visualized in the contour plots presented in Fig. 4. In the latter, the starting circular shape corresponding to 0 % global strain morphed into a hexagon-like geometry at 10 % global strain. It then follows that the lateral deformation tracks the axial counterpart for cylindrical cells but at a much shallower slope (*i.e.*, lower strain ratio). In all, the deformation behavior of a unit cell is based on the combined interactions of the geometry correspondence within the structure and strain hardening effect within the materials of cells.

The aforesaid strain contours within the field of view and the deformation of the unit cell relate to the strains at the subcellular level, specifically the deformation of the ligands within their respective coordinate system (Fig. 3). That is, the axial strains and the corresponding lateral strains (ε_{yy}, and ε_{xx}, respectively) defined along the axis of the ligand and the orthogonal direction, respectively, are local descriptors of deformation. The quasi-static uniaxial compressive loading scenario considered herein results in deformation symmetry about the vertical geometric axis of each cell, where the deformation of ligands 1, 6, and 5 are mirrored in ligands 2, 3, and 4, as shown in Fig. 3. More specifically, the deformation within ligand 2 (a diagonal strut) and ligand 3 (a vertical strut) can be considered unique. In contrast, the others are a byproduct of symmetry. Fig. 6 shows the axial and lateral ligands 2 and 3 strains for the cylindrical and hexagonal unit cells. The extracted attributes intentionally excluded the strain localization at the previously discussed nodes. Irrespective of the cell geometry, the diagonal strut exhibits a linear relationship between the lateral and axial strains, as shown in Fig. 6a. The compressive axial strain within the local coordinate system of the ligand naturally resulted in transverse strain due to the elastic properties of the material. However, increasing the reinforcement weight ratio affected the relationship between axial and lateral strains (Fig. 6b). The lateral-axial response for 20 *wt.*% glass microballoons can be described as nonlinear since the bonding between the resin and the reinforcing phase exhibits a broad variance of adhesion, ranging from fully bonded to unbonded, as reported in Ref. [40] using micrographic analysis based on scanning electron microscopy. This is also a known issue in particulate composites, affecting their global mechanical behavior [41,42]. Future research will focus on extending the models in Refs. [41,42] to account for the adhesion between glass microballoons and flexible, photocurable resins used in the current research. Moreover, it is imperative to note that calculating the strain ratio (or Poisson's ratio) from this local behavior is futile since current measurements are blind to the multiaxial state of strain and material nonlinearities. Fig. 6 also revealed two compelling observations for each configuration beyond the insight into the degree of linearity for the neat and 20 *wt.*%. First, the vertical struts displayed an intriguing behavior that was clearly pronounced when the neat resin was used for 3D printing. At the onset of deformation, the axial and the lateral strains monotonically increased to accommodate the compression in the oblique ligand. Once the latter was fully developed due to the strain localization, the axial strain started to decrease and shifted the sense into the compressive regime, while the lateral strain continued to ascend. Schematic representation within Fig. 6a illustrates the deformation mechanism discussed above. Second, the lateral and axial strain

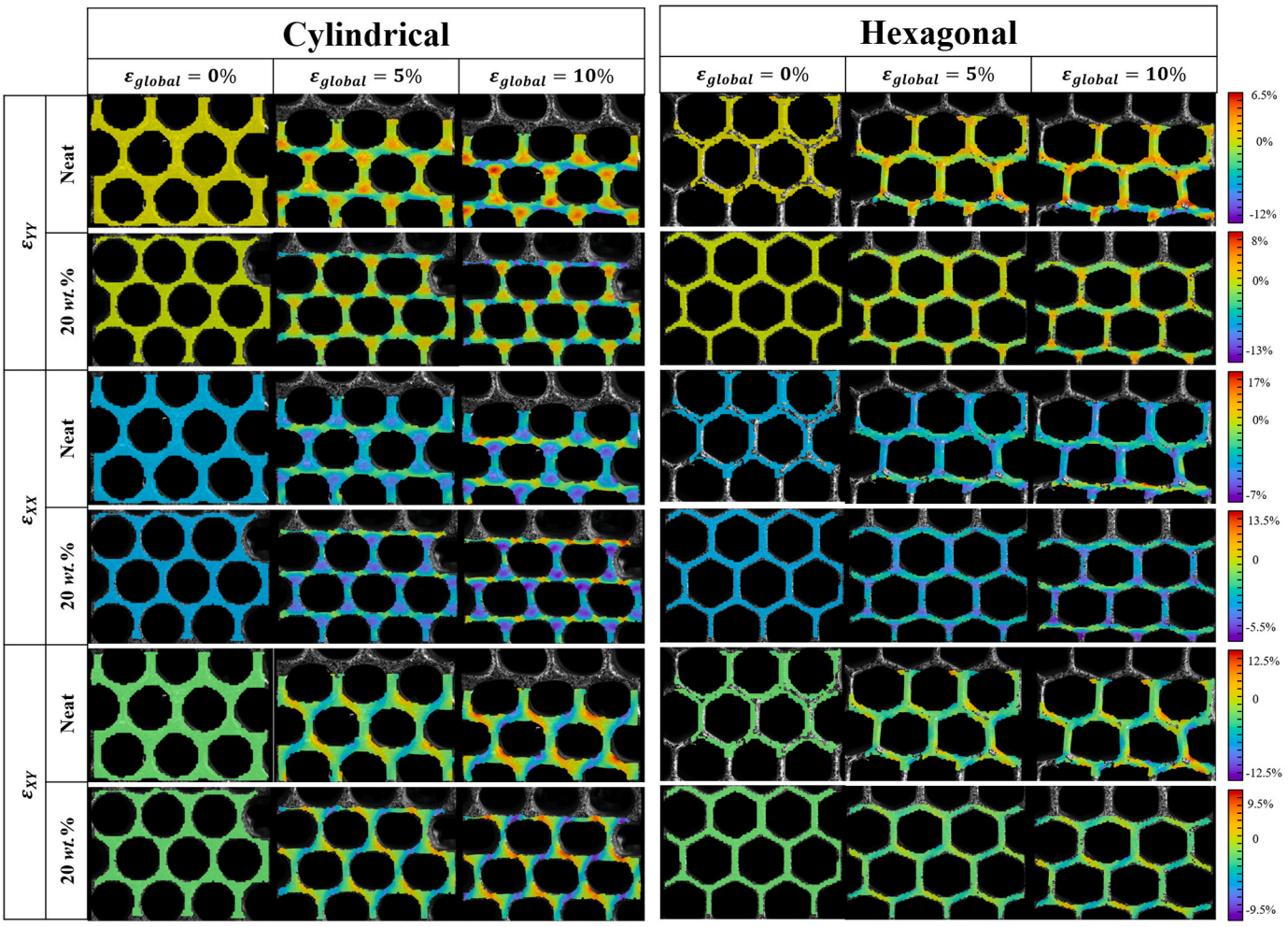

Fig. 4. Contour plots for axial, lateral, and shear components of the deformation response for cylindrical and hexagonal samples subjected to quasi-static loading (contours shown up to 10 % global strain).

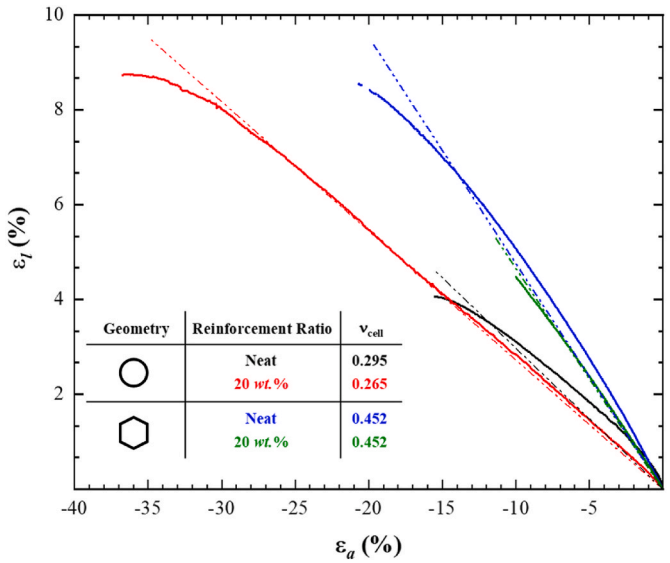

Fig. 5. Relationship between the in-plane axial (ε_a) and lateral (ε_l) deformations of representative cylindrical and hexagonal unit cell structures subjected to quasi-static compression. These responses were plotted alongside their corresponding apparent strain ratio taken as the slope of the quasi-linear fit to the response.

relationship illustrated in Fig. 6b for the cylindrical geometry is characterized by a nonlinear increase before peaking and returning in a similar manner for ligands 2 and 3. This initial regime captures the compressive deformation in the angled and axially oriented ligands before a critical compressive load was reached in the strut, and buckling occurred at the minimum cross-section of ligand 2 (promoted by the curvature of the ligand from the cylindrical unit cell). Due to the structural constraint of the honeycomb arrangement, the primary deformation mode of the second strut becomes bending, resulting in the descending regime for the lateral-axial strain ratio. The maximum axial and lateral strains experienced by each strut mapped to the elastic instabilities observed in the global stress-strain response of the composite honeycomb structures at the offset of the linear elastic region and the onset of the plateau region ($\varepsilon_{global} \sim$ 13–14 %), as reported in Ref. [40]. Overall, this associative behavior between the oblique and vertical struts demonstrates the physicality of the presented deformation field at the subcellular, cellular, and structural levels.

At the outset, the energy absorption characteristics of the 3D printed structures as a function of the cell geometry and reinforcing ratio were recently discussed in Ref. [40]. These performance metrics are recalled herein to ascertain further the future utility of these meta-structures in impact mitigation applications. The specific energy absorbed at the onset of densification ranged between *ca.* 483 J/kg and 788 J/kg for structures with hexagonal unit cells, reported at ~40 % strain. On the other hand, the specific energy absorption values for cylindrical honeycombs varied between ~420 J/kg and 811 J/kg at corresponding

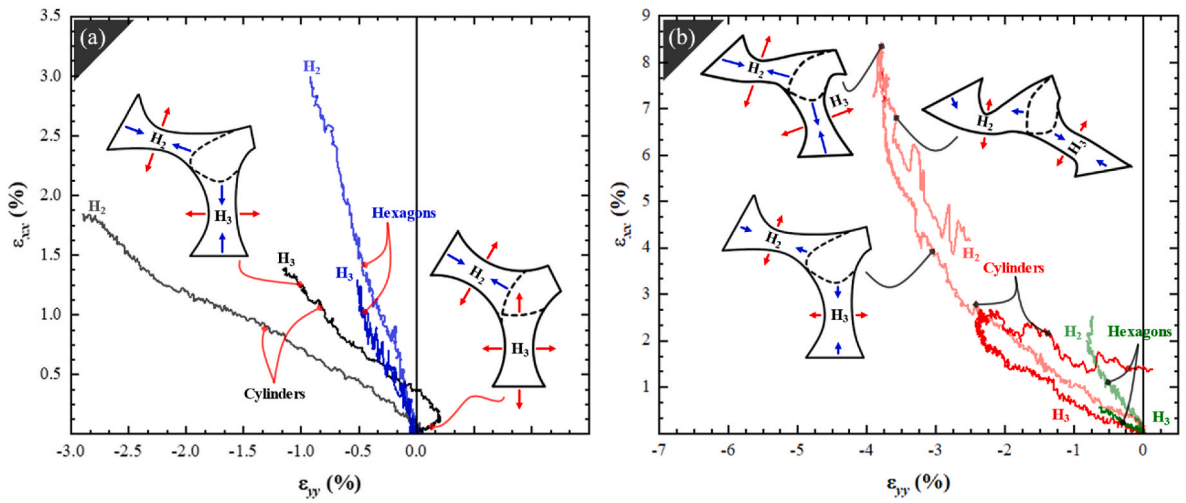

Fig. 6. Longitudinal and transverse strain responses for ligands 2 and 3 in their respective coordinate system for (a) neat and (b) 20 *wt.*% reinforced honeycomb structures under quasi-static loading.

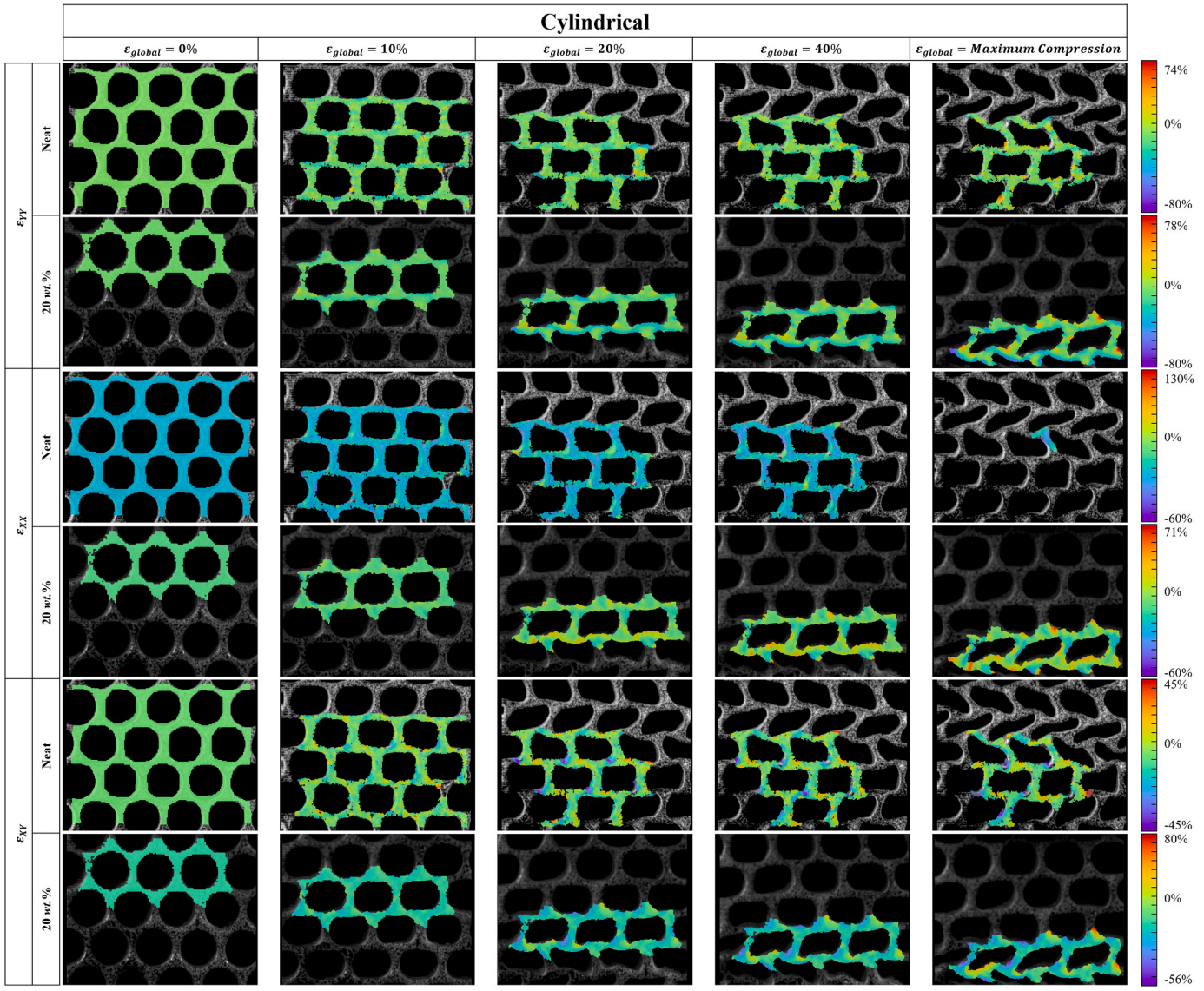

Fig. 7. Contour plots for axial, lateral, and shear components of the deformation response for cylindrical (top panels) and hexagonal (bottom panels) samples subjected to impact loading (contours shown up to maximum compression).

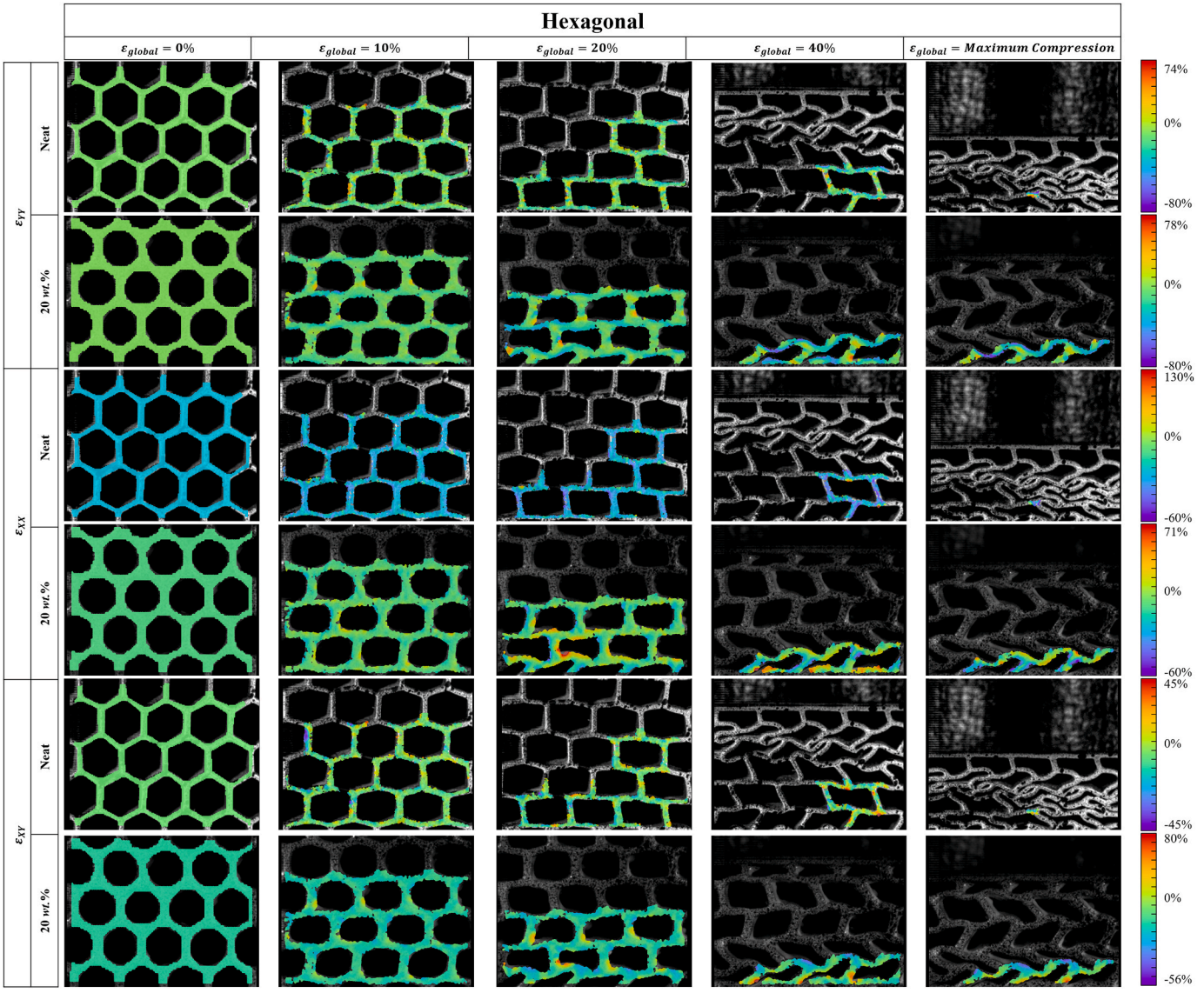

Fig. 7. (*continued*).

strains of >45 %. The reader is referred to the report by Singh et al. for a further discussion about the relationship between cell geometry, reinforcing weight ratio, and mechanical behavior of these 3D printed honeycombs [40].

3.2. Loading scenario II: drop-weight impact

The results of the DIC analysis for the dynamic testing scenario, based on an impact energy of 9.6 J from dropping a mass, are summarized in the strain contour plots shown in Fig. 7. This figure includes the in-plane strain components for the same sample configurations considered in the previous loading scenario. Additional configurations for the remaining reinforcing weight ratios are displayed in a similar figure in the *Supplementary Document*. Fig. 7 includes the axial, lateral, and shear strains (ε_{YY}, ε_{XX}, and ε_{XY}, respectively) for the cylindrical and hexagonal honeycomb structures at $\sim$ 98 s^{-1} global nominal strain rate. At the onset, it is imperative to note that the magnitudes of local strains in the current loading scenarios are, on average, nearly sevenfold higher than the quasi-static counterparts presented in the previous section. The difference between induced strain herein and those generated in the quasi-static case is attributed to (1) the increase in strain rate with impact loading compared to quasi-static loading, (2) the strain rate sensitivity of the flexible resin and its composites, and (3) the dominant structural deformation mechanism embodied in cell collapse. Another notable difference is the trackable global strain, where the field of view encompassed the entire sample throughout the impact duration. This was not the case for the quasi-static scenario discussed above, such that only a few representative cells were tracked within the field of view up to 10 % global strain, at which point the correlation was abandoned since the trackable cells moved out of view. Another point of contrast between the dynamic and quasi-static analyses is the reliability of the correlation, where the contour plots in Fig. 7 showed the resolved strains superimposed on fewer unit cells than at the starting point in the currently considered loading scenario. In the current dynamic experimental setup, the deformation was recorded with a single high-speed camera and a limited illumination source that, in turn, affected the quality of acquired images at a high strain percentage and faulted the out-of-plane deformations. In addition, trackable strain contours were also affected by image-to-image noise, low pixel density, and speckle pattern quality associated with the available high-speed photography equipment, resulting in an evaluation with a lower spatial resolution compared to the quasi-static counterpart. Despite this limitation, the measurement uncertainty associated with collecting each local strain (reported by the DIC software) was reduced to a negligible level by

removing outliers around the evaluation area.

The axial strains for the hexagonal honeycombs varied between −80 % and 74 % in the dynamic loading scenario and −80 % and 78 % for the cylindrical counterparts. Similar distributional behaviors were also observed in the lateral and shear strains, where the values are generally higher in magnitude. However, for the lateral and shear strains, the distribution appeared to be smeared over the surface of the remaining trackable cells since the primary cell collapse mechanism was accompanied by excessive cell wall bending at higher global strains. In addition, the cylindrical structures accumulated strain localization regions at sharp corners at the end of the impact scenario due to excessive deformation of the vertical struts, exemplified as significant compression and bending. Such strain localization regions were axiomatic in all explored in-plane strain components. It is worth noting that despite the excessive deformation reported in the contour plots, irrespective of the direction, the honeycombs recovered to their original geometry after a period of rest due to the compliant and time-dependent properties of the flexible resin. While anecdotal, it is essential to note that out of the forty 3D printed and impact-tested combs, only one demonstrated plastic failure and remnant plastic deformation, which was attributed to variations in the post-processing steps [40].

Similar to the quasi-static case, the axial and lateral deformations of a representative unit cell were extracted using the same method discussed above via two diametrically orthogonal line gauges. Fig. 8 correlates the axial and lateral cellular deformations, revealing a quasi-linear relationship quantified by a slope, *i.e.*, the apparent strain ratio. The cell geometry and the reinforcing weight ratio influence the relationship between the axial and lateral deformations. Comparing the apparent strain ratio as a function of the cell geometry, the hexagonal unit cell reported a value of 0.46, while 0.30 was recorded for the cylindrical cell, printed with neat resin. However, the apparent strain ratio was calculated to be 0.34 for cells fabricated with 20 *wt.*% reinforced flexible resins, irrespective of the cell geometry. Fig. 8 suggests two additional insights. First, the induced axial and lateral deformations (Fig. 8) in dynamically compressed unit cells trumps those generated in the quasi-static condition (Fig. 5) based on the reasons pertaining to the contour plots. The second is the transition between linear and nonlinear response was invoked at higher axial strains (>30 %) in the dynamic case, which was initiated at similar values in the quasi-static scenario

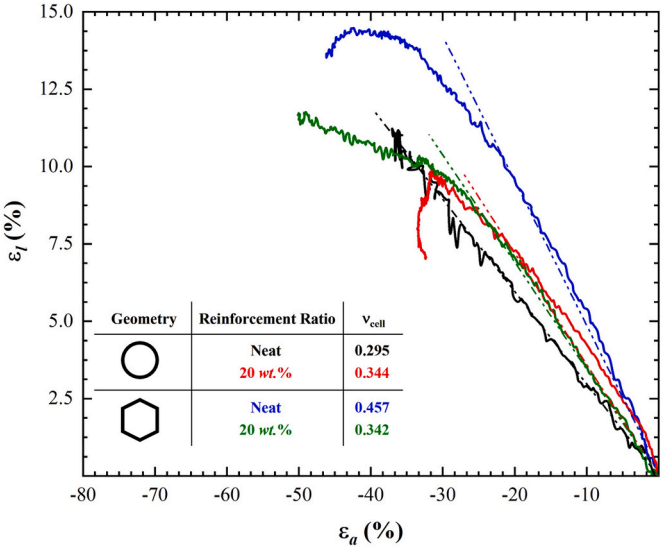

Fig. 8. Relationship between the in-plane axial (ε_a) and lateral (ε_l) deformations of representative cylindrical and hexagonal unit cell structures subjected to a drop impact loading scenario. These responses were plotted alongside their corresponding apparent strain ratio taken as the slope of the quasi-linear fit to the response.

(while showing strong dependence on the cell geometry). This transitional behavior is attributed to the cellular structure approaching the onset of densification, where cell walls will start to contact one another. It is imperative to reiterate that the resolved strains in the dynamic testing represent the full duration of the impact event. At the same time, the trackable unit cells exited the field of view within 10 % of the quasi-static compression. Finally, inference about the subcellular deformations within the individual struts was deemed unreliable due to the rapid collapse of the unit cells and the available image resolution.

Comparing the considered loading scenario affirms that the dependence of the reported deformational responses of the honeycombs at the structural and cellular level are dependent on the strain rate. Two observations evidence such affirmation. First, the samples tested under drop impact loading conditions consistently reported higher strain magnitudes than their quasi-statically tested counterparts for the same global strain of 10 %. Specifically, the axial, lateral, and shear values are four-to eight-fold, on average, higher for the impact loading scenario than the quasi-static counterpart. The dichotomy in the strains partially stems from the strain rate sensitivity of the flexible resin polymer matrix. However, it is predominantly due to the governance of excessive wall bending in the dynamic scenario on the magnitude of each developed strain, resulting in the reduction in the observable strain localization (smearing effect) illustrated in the contour plots shown in Fig. 7. The second observation is the difference between the apparent strain ratio at the cellular level, where for the neat samples, a minimal change was observed. On the other hand, the 20 *wt.*% reinforced samples had a more significant variance; the strain ratio increased by ~26 % for the cylindrical structures and decreased by ~28 % for the hexagonal combs. This discrepancy was mainly caused by the difference in the transverse strain development in the quasi-static (Fig. 5) and impact loading (Fig. 8), primarily for the 20 *wt.*% samples. The apparent strain ratio persists for each respective cell geometry for increased strain rate. Instead, an increased weight reinforcement has a pronounced effect on the development of lateral cell strain and, subsequently, on the apparent strain ratio.

4. Conclusion

This research characterized the full field deformation response of composite cellular solid structures as a function of weight reinforcement and compressive loading scenarios (quasi-static and drop-impact loading). The primary outcome of this research was the insight into the deformation state of honeycombs with cylindrical and hexagonal unit cells at the structural, cellular, and sub-cellular levels. Extensive analysis via digital image correlation was imperative to obtain these multiscale deformation patterns, revealing the relationship between the in-plane axial, lateral, and shear strain components of the structural strain contour. Subsequently, the lateral and axial deformations at the cellular level elucidated the relationship between the deformation mechanisms that accommodate the in-plane loading scenarios, irrespective of the strain rate. Finally, the sub-cellular axial and lateral strain components within the ligands of each unit cell were resolved from the strain contours through strategically defined virtual line gauges, revealing deformative relationships between adjacent ligands. The concluding observations are enumerated below.

1. Variance in the cell geometry and weight reinforcement had a strain-localization effect on the structural deformation of the composite structures.
2. Changes in the cellular strain ratio for each sample configuration illustrated a persistent geometry-driven correspondence between the lateral and axial cell strains.
3. The relationship between the ligand deformations in their local coordinate system and the global deformation was coupled by the nodal connections between unit cells and strongly influenced by geometry.

Therefore, this study characterized the structural and mechanical response of the hexagonal and cylindrical honeycombs as a function of reinforcing weight ratio, unit cell geometry, and loading-induced deformation patterns. The global response of the entire structure is dictated by the multiscale cellular distortion experienced throughout loading.

CRediT authorship contribution statement

Anil Singh: Data curation, Formal analysis, Investigation, Visualization, Writing – original draft, Writing – review & editing, Methodology. **Behrad Koohbor:** Conceptualization, Formal analysis, Funding acquisition, Methodology, Writing – original draft, Writing – review & editing. **George Youssef:** Conceptualization, Data curation, Formal analysis, Funding acquisition, Investigation, Methodology, Project administration, Resources, Visualization, Writing – original draft, Writing – review & editing.

Declaration of competing interest

The authors declare that they have no known competing financial interests or personal relationships that could have appeared to influence the work reported in this paper.

Data availability

Data will be made available on request.

Acknowledgement

The authors acknowledge the support by the National Science Foundation under Grant No. 2035663 (G.Y.) and Grant No. 2035660 (B. K.). The authors are also grateful for internal funding from San Diego State University and Rowan University. Funding from the Department of Defense (G.Y.: W911NF1410039, W911NF1810477, and W911NF231 0150) is also acknowledged. The authors also acknowledge the help of Vincent Ngo and Dr. Nha Uyen Huynh for their help in several initial aspects of the project and collecting the images.

Appendix A. Supplementary data

Supplementary data to this article can be found online at https://doi.org/10.1016/j.compositesb.2024.111208.

References

[1] Gill S, Arora H, Sheth V. On the development of Antenna feed array for space applications by additive manufacturing technique. Addit Manuf 2017;17:39–46.
[2] Nohut S, Schwentenwein M. Vat photopolymerization additive manufacturing of functionally graded materials: a review. Journal of Manufacturing and Materials Processing 2022;6(1):17.
[3] Paek SW, Balasubramanian S, Stupples D. Composites additive manufacturing for space applications: a review. Materials 2022;15(13):4709.
[4] Pazhamannil RV, Govindan P. Current state and future scope of additive manufacturing technologies via vat photopolymerization. Mater Today Proc 2021;43:130–6.
[5] Zhang F, et al. The recent development of vat photopolymerization: a review. Addit Manuf 2021;48:102423.
[6] Ashby MF, Gibson LJ. Cellular solids: structure and properties. Cambridge, UK: Press Syndicate of the University of Cambridge; 1997. p. 175–231.
[7] Jiang H, et al. Crashworthiness of novel concentric auxetic reentrant honeycomb with negative Poisson's ratio biologically inspired by coconut palm. Thin-Walled Struct 2020;154:106911.
[8] Sang L, et al. Development of 3D-printed basalt fiber reinforced thermoplastic honeycombs with enhanced compressive mechanical properties. Compos Appl Sci Manuf 2019;125:105518.
[9] Wang Z, Zhang Y, Liu J. Comparison between five typical reinforced honeycomb structures. International conference on advanced engineering materials and technology. Atlantis Press; 2015. 2015.
[10] Zeng W, et al. Fabrication method and dynamic responses of composite sandwich structure with reentrant honeycomb cores. Compos Struct 2022;299:116084.
[11] Liu Z, et al. The impact responses and failure mechanism of composite gradient reentrant honeycomb structure. Thin-Walled Struct 2023;182:110228.
[12] Pagliocca N, Youssef G, Koohbor B. In-Plane mechanical and failure responses of honeycombs with syntactic foam cell walls. Compos Struct 2022;295:115866.
[13] Xu HH, et al. Mechanical properties of aluminum foam filled re-entrant honeycomb with uniform and gradient designs. Int J Mech Sci 2023;244:108075.
[14] Hu L, Zhou MZ, Deng H. Dynamic indentation of auxetic and non-auxetic honeycombs under large deformation. Compos Struct 2019;207:323–30.
[15] Ju J, Summers JD. Compliant hexagonal periodic lattice structures having both high shear strength and high shear strain. Mater Des 2011;32(2):512–24.
[16] Qi C, et al. Quasi-static crushing behavior of novel re-entrant circular auxetic honeycombs. Compos B Eng 2020;197:108117.
[17] Song S, et al. Fabrication and mechanical behavior of an all-composite interlocked triangular honeycomb sandwich structure: experimental investigation and numerical analysis. Polym Compos 2023;44(2):833–49.
[18] Wang X, et al. 3D printing of polymer matrix composites: a review and prospective. Compos B Eng 2017;110:442–58.
[19] Malley S, Newacheck S, Youssef G. Additively manufactured multifunctional materials with magnetoelectric properties. Addit Manuf 2021;47:102239.
[20] Gr A, Sanjay M, Yogesha B. Review on comparative evaluation of fiber reinforced polymer matrix composites. Carbon 2014;4000:30.
[21] Boggarapu V, Gujjala R, Ojha S. A critical review on erosion wear characteristics of polymer matrix composites. Mater Res Express 2020;7(2):022002.
[22] Herakovich CT. Mechanics of composites: a historical review. Mech Res Commun 2012;41:1–20.
[23] Jones RM. Mechanics of composite materials. CRC press; 2018.
[24] Daniel IM, et al. Engineering mechanics of composite materials, vol. 1994. New York: Oxford university press; 2006.
[25] Ashby MF, Shercliff H, Cebon D. Materials: engineering, science, processing and design. Butterworth-Heinemann; 2018.
[26] Youssef G. Creep analysis of E-glass/vinyl-ester laminated composites for underground vault structures. Polym Compos 2020;41(9):3564–74.
[27] Pascault JP, Williams RJ. Thermosetting polymers. Handbook of polymer synthesis, characterization, and processing. 2013. p. 519–33.
[28] Youssef G. Applied mechanics of polymers: properties, processing, and behavior. Elsevier; 2021.
[29] Rulkens R, Koning C. Chemistry and technology of polyamides. In: Polymer science: a comprehensive reference. Elsevier; 2012. p. 431–67.
[30] Melton GH, Peters EN, Arisman RK. Engineering thermoplastics. In: Applied plastics engineering handbook. Elsevier; 2011. p. 7–21.
[31] Chairi M, et al. Composite materials: a review of polymer and metal matrix composites, their mechanical characterization, and mechanical properties. 2023.
[32] Baillie C, Jayasinghe R. Green composites: polymer composites and the environment. Elsevier; 2004.
[33] Compton BG, et al. Thermal analysis of additive manufacturing of large-scale thermoplastic polymer composites. Addit Manuf 2017;17:77–86.
[34] Penumakala PK, Santo J, Thomas A. A critical review on the fused deposition modeling of thermoplastic polymer composites. Compos B Eng 2020;201:108336.
[35] Hassen AA, et al. Additive manufacturing of composite tooling using high temperature thermoplastic materials. In: SAMPE conference proceedings; 2016. Long Beach, CA.
[36] Yuan S, et al. Additive manufacturing of polymeric composites from material processing to structural design. Compos B Eng 2021;219:108903.
[37] Yaragatti N, Patnaik A. A review on additive manufacturing of polymers composites. Mater Today Proc 2021;44:4150–7.
[38] Goh GD, et al. Recent progress in additive manufacturing of fiber reinforced polymer composite. Advan. Mater. Tech. 2019;4(1):1800271.
[39] Davoudinejad A. Vat photopolymerization methods in additive manufacturing. In: Additive manufacturing. Elsevier; 2021. p. 159–81.
[40] Singh A, et al. Structural performance of additively manufactured composite lattice structures: strain rate, cell geometry, and weight ratio effects. Adv Eng Mater 2023.
[41] Tohgo K, Itoh Y, Shimamura Y. A constitutive model of particulate-reinforced composites taking account of particle size effects and damage evolution. Compos Appl Sci Manuf 2010;41(2):313–21.
[42] Ravichandran G, Liu C. Modeling constitutive behavior of particulate composites undergoing damage. Int J Solid Struct 1995;32(6–7):979–90.